Journal of Power Sources 659 (2025) 238413

Contents lists available at ScienceDirect

Journal of Power Sources

journal homepage: www.elsevier.com/locate/jpowsour

High-performance sodium-ion full cell using tunnel and layered-type composite cathode

Soutan Adak [a], Ahin Roy [a], Susanta Banerjee [a], Jeng-Kuei Chang [b,c,*], Subhasish Basu Majumder [a,**]

[a] Materials Science Centre, Indian Institute of Technology, Kharagpur, 721302, W.B., India
[b] Department of Materials Science and Engineering, National Yang Ming Chiao Tung University, 1001 University Road, Hsinchu, 30010, Taiwan
[c] Department of Chemical Engineering and R&D Center for Membrane Technology, Chung Yuan Christian University, 200 Chung Pei Road, Taoyuan, 32023, Taiwan

HIGHLIGHTS

- $Na_{0.44}MnO_2$ (NMO) cathode synthesized via modified autocombustion method.
- Sheet-to-rod evolution in NMO with sodium-ion diffusion pathways elucidated.
- NMO–NFM blend shows synergistic effect with higher rate capability.
- NMO composite–hard carbon full cell assembled and tested at 1C.

GRAPHICAL ABSTRACT

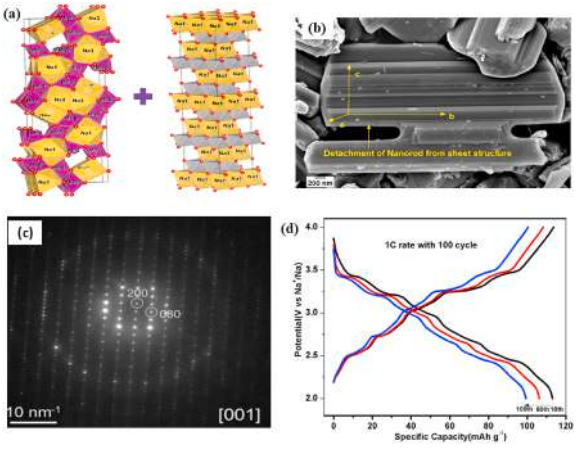

ARTICLE INFO

Keywords:
Tunnel-structured $Na_{0.44}MnO_2$
Layered-structured $Na(Ni_{1/3}Fe_{1/3}Mn_{1/3})O_2$)
Auto combustion synthesis
Composite cathode
Sodium-ion full cell

ABSTRACT

$Na_{0.44}MnO_2$(NMO) powders are synthesized by auto combustion. At lower calcination temperature, carbothermal reductive environment preserves lamellar Birnessite type slab of NMO. A stress induced mechanism is proposed to explain the splitting of the lamellar nanosheet to NMO rods. TEM analyses confirm that the diffusion distance for Na^+ ion extraction is much shorter than the growth direction to facilitate the extraction of Na^+ from NMO lattice. Due to facile extraction of Na^+ ions, remarkable 1st charge capacity ~96 $mAhg^{-1}$ is obtained in NMO cathode. Composite of NMO and TiO_2 coated $Na(Ni_{1/3}Fe_{1/3}Mn_{1/3})O_2$ (NFM) is made as a novel cathode for Na ion rechargeable cells. At 1C the discharge capacity of 0.7 NMO–0.3 NFM composite is reported to be 113 $mAhg^{-1}$ with a capacity retention of ~80 % after 100 cycles. The composite cathode also exhibits superior rate performance with a discharge capacity ~66 $mAhg^{-1}$ at 15C rate. In a voltage window of 1.0–4.0V, the discharge

* Corresponding author. Department of Materials Science and Engineering, National Yang Ming Chiao Tung University, 1001 University Road, Hsinchu, 30010, Taiwan.
** Corresponding author.
E-mail address: subhasish@matsc.iitkgp.ac.in (S.B. Majumder).

https://doi.org/10.1016/j.jpowsour.2025.238413
Received 8 June 2025; Received in revised form 29 August 2025; Accepted 14 September 2025
Available online 25 September 2025

capacity of hard carbon and 0.7NMO – 0.3NFM full cell is measured to be 133 $mAhg^{-1}$ and 109 $mAhg^{-1}$ at 0.1 and 1C respectively. After 100 cycles, at 1C rate, we have reported 80 % capacity retention of the full cell.

1. Introduction

Significant research activities are being pursued on a variety of materials as positive electrodes for sodium ion rechargeable cells. These materials can broadly be classified into transition metal oxides, poly-anionic compounds, Prussian white/Prussian blue analogue, and organic cathode materials [1]. Among these classes of materials manganese-based sodium manganese oxides (Na_xMnO_2, $0 \leq x \leq 1.0$) have found to be attractive because of the abundancy of cheaper manganese precursors. When $0.22 \leq x \leq 0.44$, Na_xMnO_2 crystallizes into tunnel structure (TS), whereas $0.66 \leq x \leq 1.0$ results fully layered structure (LS). However, a mixer of TS and LS is formed when $0.44 \leq x \leq 0.66$.

One of the major drawbacks of the tunnel structured NMO is that yields lower charge capacity. Schematic crystal structure of $Na_{0.44}MnO_2$ (NMO) (analogue of $Na_4Mn_9O_{18}$) is shown in Fig. S1 (a) of the supporting document which marks three Na^+ positions (Na1, Na2, and Na3) and five Mn ion positions Mn1, Mn2, and Mn5 (Mn^{4+}),Mn3, Mn4 (Mn^{3+}) in NMO cell. In a voltage window 4.0–2.0 V Na/Na^+, sodium ions can reversibly be de-inserted/inserted (during charge/discharge respectively) mostly from Na2 and Na3 crystallographic sites. Although Na2 and Na3 can accommodate more Na^+ ions [2,3], maximum up to 0.22 Na^+ can be extracted during 1st charge. Therefore, the 1st charge capacities have always been reported $\leq$60 $mAhg^{-1}$ in various recent literature reports [4–6]. Due to such low first charge capacity, hard carbon–NMO–based full cell charge capacity has been reported to be only 36 $mAhg^{-1}$ [7]. It remains therefore of prime importance to increase the 1st charge capacity of NMO and we have categorized various strategies adopted in literature to increase its 1st charge capacities. These strategies are (a) presodiation [8], (b) adaptation of engineered synthesis, (c) doping Mn ions with suitable cations. However, process complexities and optimization of pre–sodiation time render it difficult for roll–to-roll coating during cell making [9]. D.Wang et al. [10] has reviewed the synthesis routes to make TS type NMO. Along with solid state and solution-based routes, specialized synthesis, including but not limited to electrospinning, spray pyrolysis, solution combustion and molten salt-based techniques, have also been used. However, in these reports, either the 1st charge capacities not explicitly been reported or it has been reported to be $\leq$ 60 mAh/g.

In Na_xMnO_2 ($0.22 \leq x \leq 1.0$), crystallization of tunnel structured material is preferred over layered structured cathode due to the moisture insensitivity of the later. Thus, due to its moisture sensitivity, poor electrochemical stability, especially upon repeated cycling, has been reported in layered type Na_xMnO_2. As compared to layered structure, NMO with tunnel structure is preferred for its lower moisture sensitivity and facile Na^+ ion extraction. However, stringent composition control ($0.22 \leq x \leq 0.44$) is required for the crystallization of Na_xMnO_2 (analogue $Na_4Mn_9O_{18}$) into tunnel structure (TS). It is well known that when $0.66 \leq x \leq 1.0$, fully layered structure (LS) crystallizes, whereas when $0.44 \leq x \leq 0.66$ a mixer of TS and LS results.

To improve the rate performance of pure NMO, optimization of synthesis parameter found to have immense influence. Solution auto–combustion has been reported to be highly effective to synthesize tunnel structured $Na_{0.44}MnO_2$. In auto combustion synthesis one can tune the phase purity, morphology, tunnel structure, and length: diameter (L/D) ratio of the synthesized nano–rods to yield superior electrochemical performances. Thus, by optimizing the fuel: oxidizer ratios though higher capacity ~100 $mAhg^{-1}$ is reported at 4C even after 300 cycles for solution combustion synthesized $Na_{0.44}MnO_2$ [11]; its 1st charge capacities remained low ($\leq$60 $mAhg^{-1}$). Single or dual dopant induced TS to LS phase transition (for example in $Na_{0.44}Mn_{0.94}W_{0.01}Al_{0.05}O_2$) has been reported to enhance reversible as well as 1st charge capacity and smoothen the resultant voltage transient by suppressing the Na^+ ion vacancy ordering upon cycling. [12]. Thus, the reversible capacities of both W and Al co–doped NMO are reported to be much higher (~150 $mAhg^{-1}$ measured at 1C) and as compared W doped NMO (85 $mAhg^{-1}$). The layered structured Al/W co–doped cathode yields superior capacity retention (121 $mAhg^{-1}$, i.e 80 %) after 200 cycles measured at 1C. We feel that yielding higher capacity utilizing the dopant induced tunnel to layer structural conversion is not an ideal strategy to improve the overall performance of $Na_{0.44}MnO_2$ cathode.

In the present work we have proposed a mechanism of the formation of tunnel structured NMO prepared using auto–combustion synthesis. By optimizing the fuel: oxidiser ratio during auto–combustion synthesis, we provided a mechanistic view to achieve superior 1st charge capacity of the synthesized NMO due to the facile extraction of Na^+ ions not only from Na2 and Na3 crystallographic sites but also at least part extraction from otherwise inactive Na1 sites confined in pentagon type regions. Limited attempts have been made to make composite of NMO with other cathode materials to improve the 1st charge capacities of NMO. The use of composite strategies that integrate different materials has been extensively investigated as an effective means to enhance the overall performance of electrode materials [13–16].Thus, Liu et al. reported that in Prussian blue analogue $Na_2Fe(Fe(CN)_6)$ (PBA) – $Na_{0.44}Mn_{0.85}Ti_{0.15}O_2$ (NMTO) composite (20:80 M ratio) [17], 1st charge capacity in half – cell configuration is ~95 $mAhg^{-1}$ (measured at C/10 rate). At same rate the 1st charge capacity of $Na_{0.44}Mn_{0.85}Ti_{0.15}O_2$ was reported to be only ~55 $mAhg^{-1}$. The improvement in 1st charge capacity in PBA–NMTO composite was explained to be due to a novel sodium compensation strategy. In another study, $Na_{0.44}MnO_2$ – $Na_2Mn_3O_7$ (31:69 phase ratio) heterojunction was prepared using microwave-assisted solution synthesis [18]. The 1st charge capacity of the composite was reported to be ~125 $mAhg^{-1}$ (@200 mAg^{-1}). However, in most of these studies, full cell characteristics of the composite cathodes have not been reported [18,19]. In view to this we thought it will be fruitful to find a suitable strategy to increase the 1st charge capacity above the usual charge capacities reported in tunnel type $Na_{0.44}MnO_2$ cathode in a half cell configuration; avoiding the tunnel to layer phase transition. Doping in layered oxide is found to be an efficient strategy to improve the electrochemical performance of parent materials. Thus, the electrochemical performance of $NaCrO_2$ is found to be grossly improved by Ni^{2+} doping [20]. Incorporation of Ni^{3+}, and Fe^{3+} in $NaMnO_2$, replacing part of Mn^{3+}, also yield superior electrochemical performances [21]. Thus, to further enhance the 1st cell charge capacity, we propose to investigate the electrochemical performance of tunnel–layer composite cathode (viz. 0.7 $Na_{0.44}MnO_2$ (NMO) – 0.3 $Na(Ni_{1/3}Fe_{1/3}Mn_{1/3})O_2$)(NFM)) prepared by a mixing route. The schematic crystal structure of NFM is shown in Fig. S1(b) of the supporting document. The composite formation is expected to be beneficial for both the constituents. First, auto–combustion synthesized NMO favors facile Na^+ diffusion to improve rate performance and in conjunction it acts as pillar to retard structural degradation of commercial TiO_2 coated NFM upon prolonged cycling. In addition, NFM, depending on its contents raise the nominal voltage and capacity to increase the energy density of composite cathode as compared to the NMO counterpart. It is expected that the 1st charge capacity of the NFM half–cell would further be increased as compared to the NMO half-cell. To the best of our knowledge, the strategy of making a composite of TS NMO and LS NFM has not yet been reported. In addition, we have also demonstrated the electrochemical characteristics of hard carbon –$Na_{0.44}MnO_2$ based full cell in CR2032 coin cell configuration. Such full cell characteristics have hardly been

reported.

2. Experimental

2.1. Powder synthesis

Auto combustion synthesis was adopted to prepare $Na_{0.44}MnO_2$ powders. The precursors, sodium nitrate and manganese acetate, were used as received. To prepare a 5 g batch, a stoichiometric amount of the precursors was dissolved in deionized water with continuous stirring. Manganese acetate was converted to nitrate by adding nitric acid to the aqueous solution. The conversion reaction is as follows:

$$Mn(CH_3COO)_2 + 2HNO_3 \rightarrow Mn\ (NO_3)_2 + 2CH_3COOH \quad [1]$$

In the auto-combustion synthesis, nitrate salts are preferred as effective oxidizers. Citric acid was used as fuel. The pertinent reaction is

$$0.44\ NaNO_3 + Mn\ (NO_3)_2 + n\ C_6H_8O_7 + (4.5n - 2.66)\ O_2 \rightarrow Na_{0.44}MnO_2 + 6n\ CO_2\uparrow + 4n\ H_2O + 1.22\ N_2\uparrow \quad [2]$$

The value of 'n' (moles of citric acid), can be adjusted to control the fuel to oxidizer ratio (f) during auto combustion synthesis. The surface morphologies are reported to be controlled by changing the value of f [11]. In the present work f is selected to be 1.11 and moles of citric acid (n) is used to be 1.6. Use of excess fuel is expected to act as an extra carbon source to induce carbothermal reductive environment during powder synthesis. As has been explained later, the reductive environment is beneficial to preserve lamellar Birnessite-type slab even after high-temperature calcination. Subsequently, ethylene glycol (1:2 M ratio of the oxidizers) was added to the solution, which acts as a stabilizing agent to ensure uniform mixing of the constituent ions. The resultant solution was continuously stirred at 80 °C for 45 min. The temperature was further increased to 120°C to form a clear gel. The heating was continued further to initiate auto combustion of the gel to form fluffy black powder. The powder was calcined at 900°C for 12 h to form crystalline $Na_{0.44}MnO_2$ powder.

To make composite cathode, 70 wt % tunnel-type calcined $Na_{0.44}MnO_2$ powder was mixed with 30 wt % commercial TiO_2 coated layered (O3 type) $NaNi_{1/3}Fe_{1/3}Mn_{1/3}O_2$ powder. Initially this powder was hand mixed in a mortar pestle. The hand mixed powder was mixed again in a vacuum mixer (MSK-SFM-07, MTI Corporation, USA) for 1 h.

2.2. Material characterization

X ray diffractograms of cathode powders were recorded using a powder diffractometer (Empyrean, Malvern Panalytical, UK) employing Cu Kα radiation. The surface morphology of the cathode powders was investigated using a FESEM microscope (Gemini 500 series, ZEISS, Germany) employing electron gun voltage of 5 kV, and a secondary electron in-lens detector. Energy dispersive X-ray spectroscopy was performed for compositional analysis of the cathode powders. The crystal structure analysis was carried out using high-resolution transmission electron microscopy. The powder $Na_{0.44}MnO_2$ samples were dispersed in isopropanol through a sonication in a bath sonicator for 30 min. A 20 μL drop of the dispersion was suspended on a carbon coated 400-mesh Cu grid followed by drying of the grid in vacuum oven for 6 h. Once dried, the sample was subjected to imaging in a 300 kV double-corrected JEOL Grand ARM microscope fitted with an EDS detector.

2.3. Electrochemical characterization

Electrochemical characteristics of the synthesized $Na_{0.44}MnO_2$ and $0.7Na_{0.44}MnO_2$–$0.3Na\ (Ni_{1/3}Fe_{1/3Mn1/3})O_2$ composites were investigated by fabricating CR2032 type coin cells both in half – cell (using Na negative electrode) and full – cell (using hard carbon negative electrode) configurations. For making electrodes a slurry was prepared by vacuum mixing of 80 wt% active material (cathode/anode powders), 10 wt% carbon black (conducting agent) and 10 wt% polyvinylidene fluoride (binder) dissolved in N–methyl pyrrolidone (NMP) solvent. The slurry was coated on aluminum foil using a commercial tape casting unit (BS-AFA-II, ZHIK Energy, China).The coating was dried overnight in a vacuum oven kept at 80°C. Electrodes (Φ ~ 20 mm) were cut using a disc cutter and CR2032 type coin cells were fabricated inside a moisture and oxygen controlled (<0.5 ppm) glove box (Labstar, MBraun Inc., Germany). In half–cell configuration Na was used as negative electrode; in full cell configuration we have used hard carbon electrode to make the coin cells. The negative electrode was tape cast on aluminum foil using a slurry made of 93 wt% hard carbon powder (Kurray type 3 commercial grade), 3.5 wt% carbon black, and 3.5 wt% PVDF binder dissolved in NMP. 1M sodium hexafluorophosphate ($NaPF_6$) salt dissolved in diglyme (DG) was used as electrolyte. A Celgard 2400 polypropylene membrane, soaked in electrolyte served as the separator.

The cyclic voltammetry of the electrodes in half – cell configurations were measured employing a voltage scan rate ranging 0.05 mVs^{-1} to 0.7 mVs^{-1} using a potentiostat – galvanostat system (BCS -815 Series, Biologic, France). Using a battery cycler (CT-4008Tn, Neware, China), galvanostatic charge-discharge measurements were performed in the voltage range of 2.0–4.0 V for the half-cell and 1.0–4.0 V for the full cell. The same equipment was also used to characterize the cycleability and rate performances of half and full cells.

3. Results and discussion

3.1. Structure and growth analyses

Fig. 1 shows the X–ray diffraction patterns of (a) $Na_{0.44}MnO_2$, (b) commercial TiO_2 coated $Na(Ni_{1/3}Fe_{1/3}Mn_{1/3})O_2$, and (c) 0.7 $Na_{0.44}MnO_2$–0.3 $Na(Ni_{1/3}Fe_{1/3}Mn_{1/3})O_2$ composite powders. The orthorhombic sodium manganese oxide (space group Pbam) diffraction peaks (Fig. 1(a)) are indexed with JCPDS card No. 27–0750. The space group of layered sodium nickel iron manganese oxide is R3-m and it is indexed with JCPDS card No. 25–0819 (Fig. 1(b)). The XRD pattern of 0.7 $Na_{0.44}MnO_2$ – 0.3 Na $(Ni_{1/3}Fe_{1/3}Mn_{1/3})O_2$ composite powder (Fig. 1 (c) is indexed in accordance with Fig. 1(a) and (b). In Fig. 1(c) the diffraction peaks from the tunnel type NMO phase are marked with asterisks. Unlike reported by others for auto–combustion synthesized $Na_{0.44}MnO_2$ [11] our NMO powder is phase pure and free from Mn_2O_3 impurity phase (JCPDS 71–0636). This indicates proper stoichiometry control of Na/Mn atomic % obtained by optimizing the fuel: oxidizer ratio during auto – combustion synthesis.

Fig. 2 (a) shows the surface morphology of calcined $Na_{0.44}MnO_2$ powder. The morphology resembles solid rods of different L/D ratios. He et al. [22] postulated that as compared to such unidimensional particles, growth of thinner bi–dimensional Birnessite nanoplates, grown perpendicular to the facile Na^+ ion extraction/insertion pathways, yield lower surface defect concentrations, increase tap density (for uniform electrode coating on current collector) and faster Na^+ ion diffusion to increase the rate performance. Li et al. [23] claims that Birnessite nanoplate has layered structure, formed of edge shared MnO_6 octahedra layers with Na^+ cations (and H_2O molecules) occupy interlayer space. Goff et al. [24] reported that during sol – gel synthesis of lamellar Birnessite (composition $Na_{0.45}MnO_{2.14}$,$0.76H_2O$, formed at temperature <400°C) is transformed into a tunnel structure (composition $Na_{0.45}MnO_{l.89}$) at calcination temperature >600°C.Using a citric acid based wet chemical synthesis Xu et al. [25] also reported the formation of solid rod like morphology of $Na_{0.44}MnO_2$ calcined at 900°C for 15 h. They termed it as "ultra–long $Na_{0.44}MnO_2$ submicron slab of >20 μm length, 1 μm width and 0.1–0.2 μm thickness. He et al. [22] reported a template assisted sol–gel route to yield thinner lamellar $Na_{0.44}MnO_2$ slabs. Polystyrene was used as extra carbon source to induce carbothermal reductive environment to preserve lamellar Birnessite type slab even after high temperature calcination.The magnified image of calcined

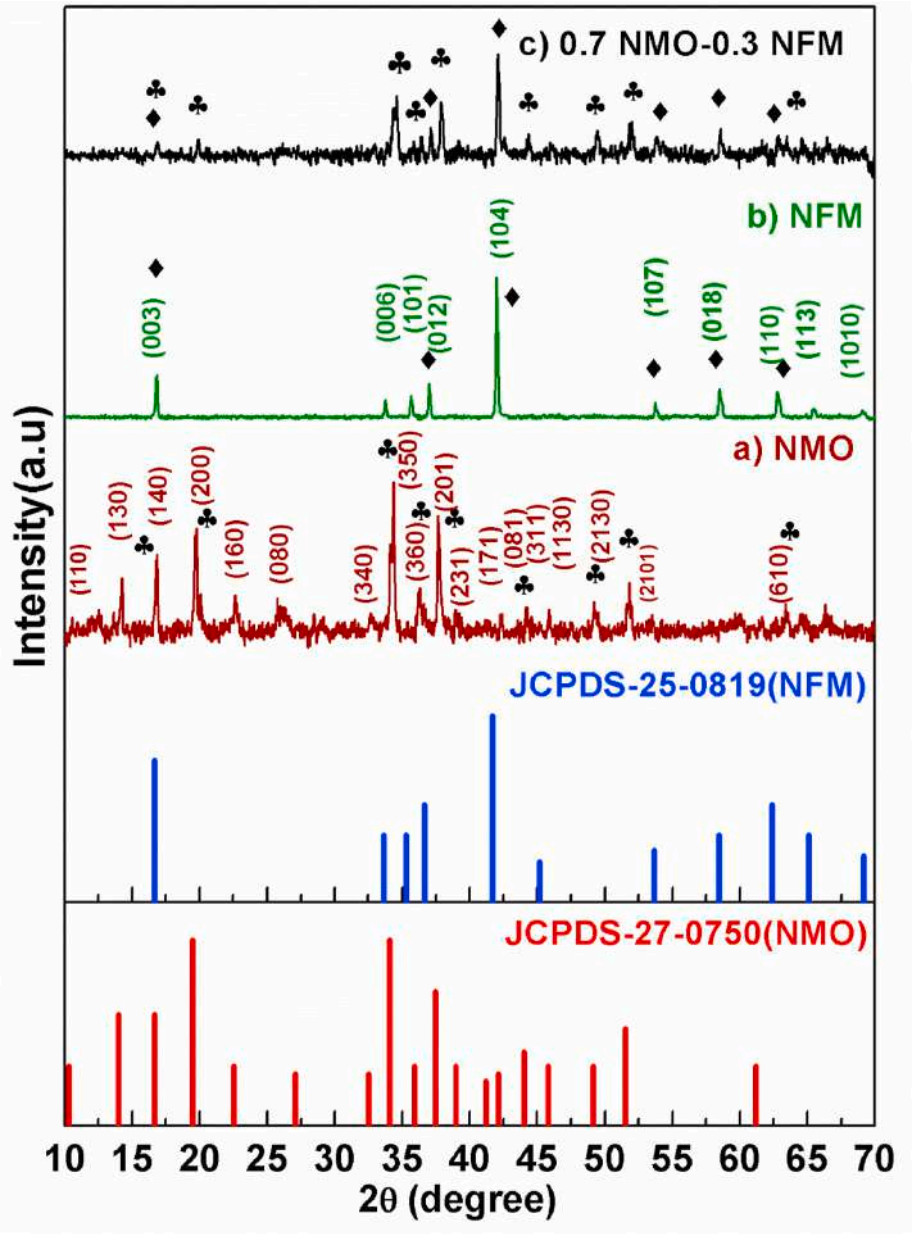

Fig. 1. X–ray diffraction patterns of (a) $Na_{0.44}MnO_2$, (b) commercial TiO_2 coated $Na(Ni_{1/3}Fe_{1/3}Mn_{1/3})O_2$, and (c) 0.7 $Na_{0.44}MnO_2$ – 0.3 $Na(Ni_{1/3}Fe_{1/3}Mn_{1/3})O_2$ composite powders. The diffraction peak positions of orthorhombic sodium manganese oxide (space group Pbam) (JCPDS card No. 27–0750) and rhombohedral layered sodium nickel iron manganese oxide (space group R3-m) (JCPDS card No. 25–0819) are also marked.

$Na_{0.44}MnO_2$ rod, synthesized in the present work, is shown in Fig. 2(b). The magnified image clearly shows that even after high temperature calcination the remaining of lamellar Birnessite is still visible in the micrograph. The conversion mechanism of lamellar Birnessite to tunnel structured $Na_{0.44}MnO_2$ solid nanorods is not well understood and we feel that in many of the reports, the growth mechanism has been mis-interpreted. In many of reports, [001] direction (along the length of the nanorod) has been reported as favorite direction for crystal growth [26, 27]. Had the growth direction been parallel to the direction of S shaped channel of Na^+ ion extraction/insertion, the long distance of the Na^+ diffusion pathway would significantly deteriorate the rate performance [22]. Contrary to the popular notion of the growth of nanorod along [001] direction, we propose alternate growth mechanism of nanorods as observed in Fig. 2(a). The nanorod formation occurs from the lamellar Birnessite; formed as an intermediate phase during low temperature calcination (see Fig. S2 of the supporting document). As shown in Fig. S2 (a), after auto combustion, large shaped lamellar regions are identified. In some regions of such lamella growth of nanocrystalline particles is apparent. When calcined at 400°C, growth of particles in these lamellar regions is readily identified (Fig. S2 (b)). With further increase of the calcination temperature (600°C), nanorods form from these lamellar Birnessite (Fig. S2 (c)). Some particulate regions are still visible in Fig. S2 (c). With further increase of calcination temperature 900°C nanorods are found to be delineated from the lamellar Birnessite (Fig. S2 (d)). In line with the schematic reported in Ref 25, the growth direction of these nanorods is along [010] (marked as b axis in Fig. 2(b)) whereas the Na^+ extraction/insertion would occur along [001] which would be much shorter than the growth length (estimated L/D ratio of the shown nanorod is ~6).

The low magnification TEM image of the rods is shown in Fig. 3 (a). HRTEM imaging on a rod readily ends up on [001] zone axis, as shown in Fig. 3 (b), with fringe spacings of 3.2 Å and 4.5 Å, respectively

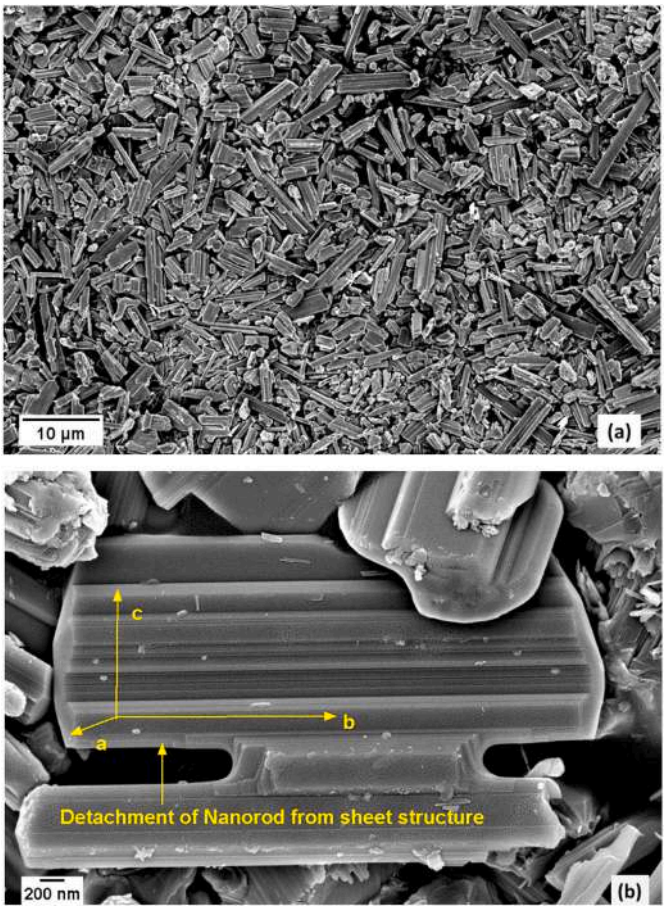

Fig. 2. Surface morphologies of (a) $Na_{0.44}MnO_2$ powders calcined at 900°C for 12 h. (b) Magnified image of the calcined powder showing the Birnessite nanoplate. The growth direction of the nanorod is along 'b' axis, whereas Na^+ ions diffuse along 'c' axis marked. The splitting of a nanorod from the nanosheet is also marked in the micrograph.

corresponding to the (080) and (200) planes. Between the two, the (080) planes are stacked along the growth direction of the rod, thus depicting [010] or the b-axis to be the growth axis. This is not too surprising, as the orthorhombic $Na_{0.44}MnO_2$ structure has a large anisotropy along the b-direction. In selected area electron diffraction, as shown in Fig. 3 (c), the obtained pattern is readily on the [001] zone axis, (similar to that of the HRTEM image.). The synthesized rods have a dark contrast, depicting its thickness. Moreover, the HAADF-STEM image shown in Fig. 3 (d), in conjunction with the low-magnification image, hints towards the layered structure of the rods along the viewing direction. The EDS analysis, done at different locations of the sample shows presence of Na, Mn and O in the sample (Fig. 3 (d)). The atomic concentration of Na/Mn is 0.43:1.0, and O/[Na + Mn] is estimated to be 2.22 using STEM – EDS.

As postulated by Li et al. [23], a stress induced mechanism can explain the splitting of the lamellar nanosheet (marked in Fig. 2(b)) to $Na_{0.44}MnO_2$ nanorods of various L/D ratios. As mentioned earlier, during solution-based synthesis lamellar Birnessite formed as intermediate phase at temperature <400°C. During high temperature calcination Mn^{3+} ions of Birnessite phase undergo a disproportionate reaction to form Mn^{4+} and Mn^{2+} ions. Mn^{2+} ions and oxidized during calcination in air ambient to form shared MnO_6 octahedra and the induced strain weakens the Birnessite layers. Eventually, as shown in Fig. 2(b), due to the in-plane stress, high energy density of defects and stacking fault the nano sheet splits into nanorods. As marked in Fig. 2(b), nanorods are shown which is almost split from the nanosheet structure but still adhered to it. The growth direction of the sheet is different from the direction of Na^+ extraction/insertion. The diffusion distance for Na^+ ion extraction is much shorter than the growth direction to facilitate the extraction of beyond 0.22 Na^+ from $Na_{0.44}MnO_2$ lattice. It is therefore expected more than 60 $mAhg^{-1}$ capacity may be achieved from auto – combustion synthesized sodium manganese oxide.

3.2. Electrochemical performance of $Na_{0.44}MnO_2$

Fig. 4 (a) shows the cyclic voltammograms of $Na_{0.44}MnO_2$ recorded after the completion of three charge – discharge cycles (forming cycles) measured in the voltage window of 2.0–4.0 V using voltage scan rates of 0.05–0.7 mVs^{-1}. Like other literature reports, appearance of six pairs of redox peaks denote different extraction/insertion steps of Na^+ ions from three different crystallographic locations (Na1, Na2, and Na3) of $Na_{0.44}MnO_2$ lattice. For all these recorded CVs marginal voltage difference (ΔV) between oxidation and reduction peaks are indicative to lower polarization effect [25]. Chae et al. [28] tried to understand sodium storage mechanism in NMO by powder X–ray Rietveld refinement and Fourier synthesis map analysis in conjunction with bond–valence–sum–difference maps (BVSMs) and barrier energy calculations based on density functional theory (DFT). Electron densities obtained by Fourier synthesis of XRD data helped them to identify Na^+ ion insertion content range from different crystallographic sites. Further using BVSMs in conjunction with DFT calculations Na1–Na1 (386 meV) diffusion energy barrier was found to be much higher than Na2–Na2 (216 meV), Na2–Na3 (241 meV) or Na3–Na3 (194 meV) diffusion energies. It is therefore postulated that Na2 and Na3 sites have major contribution for the redox reactions shown in the cyclic voltammogram as compared to Na1 sites. Considering Na1 sites are confined in pentagon type region and Na2 and Na3 sites are withing 'S' type tunnel (see Fig. S1(a)), a hopping mechanism of Na^+ ion transport might still be possible between Na1–Na1 sites, as compared to easier diffusion pathways in the 'S' type tunnel. Corresponding to each of the reduction peaks of CVs, using Randles – Sevcik relation, we have estimated the corresponding slopes from the linear fit of the reduction peak currents and square root of the used CV scan rates (Fig. S3). The highest slopes of the linearly fitted curves indicate the Na^+ ion extraction from either Na2 or Na3 crystallographic sites, whereas the lowest slope might indicate extraction from Na1 crystallographic sites.

Fig. 4(b) shows the charge discharge profiles of Na–$Na_{0.44}MnO_2$ half-cell at 1st and 4th charge – discharge cycles measured at C/10 rate. It is remarkable to achieve 1st charge capacity ~96 $mAhg^{-1}$ which is thought to be facile diffusion (due to shorter diffusion distance as marked and explained in Fig. 2(b)) of Na2, Na3 and probably from Na1 site as well. The electrochemical reaction corresponding charge can be estimated as

$$Na_{0.44}MnO_2 \rightarrow Na_{0.09}MnO_2 + 0.35e^- + 0.35Na^+ \quad [1]$$

Estimating the slopes from Randles – Sevcik analyses (outlined in the preceding paragraph) tallying it with the measured discharge capacities; we have marked range of Na^+ ions inserted at corresponding crystallographic sites of Na_xMnO_2 positive electrode. The tentative electrochemical reactions during each plateau of the discharge profile have also been marked in Fig. 4(c). Table 1 compare the electrochemical performances of prepared $Na_{0.44}MnO_2$ with the ones reported in recent literatures. Facile synthesized $Na_{0.44}MnO_2$ of the present work exhibits good electrochemical performance.

3.3. Electrochemical performance of Na $(Ni_{1/3}Fe_{1/3}Mn_{1/3})$ O_2

Na layered oxides are classified P2 or O3 type depending on Na ion coordination (P = prismatic and O = octahedral) and oxygen stacking sequence (2 = ABAB ….and 3 = ABCABC ….) [29]. The X–ray diffraction pattern (Fig. 1(b)) is found to be phase pure. The charge–discharge characteristics of commercial TiO_2 coated $Na(Ni_{1/3}Fe_{1/3}Mn_{1/3})O_2$ (NFM) has been shown in Fig. 5. The cycleability of NFM is shown in the

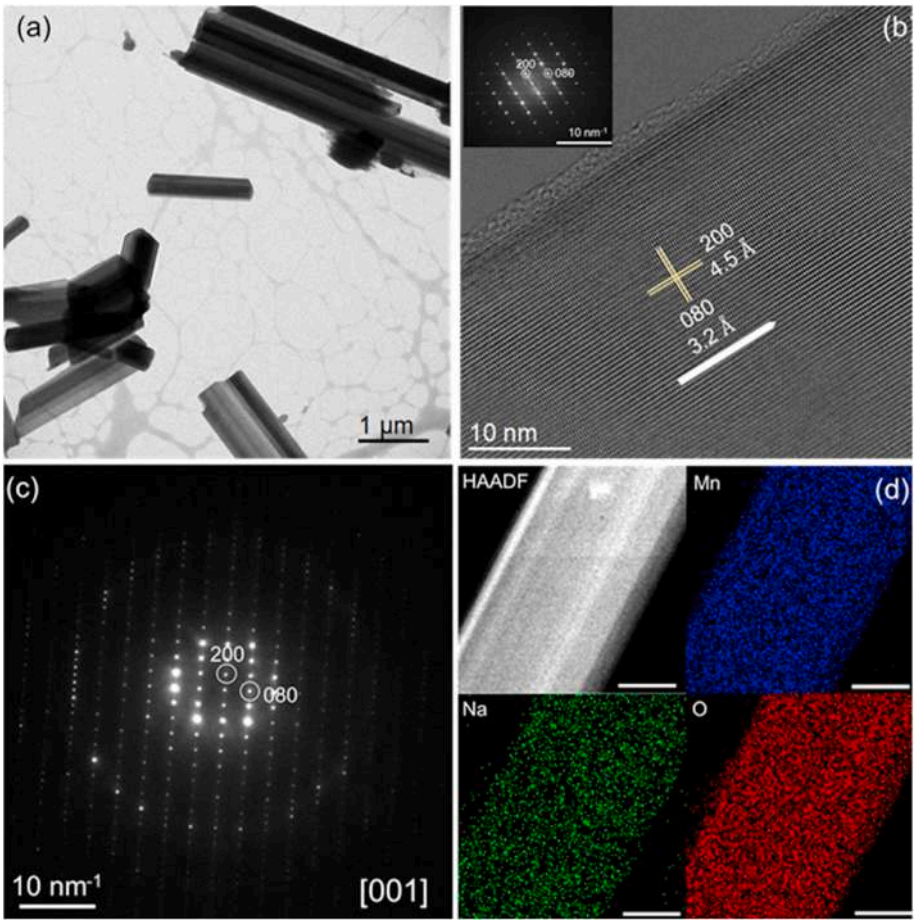

Fig. 3. (a) Low magnification TEM image of the synthesized $Na_{0.44}MnO_2$ microrods (b) HRTEM of a single rod shows the planar spacings of 3.2 Å and 4.5 Å, respectively corresponding to (008) and (200) planes – confirming the growth direction to be the [010], perpendicular to the (080) planes; (c) SAED pattern recorded from a thinner rod readily ends up on a [001] zone axis, with the spots corresponding to (0b0) and (a00) planes; (d) shows the HAADF-STEM image and the elemental EDS maps of Mn, Na and O.

inset of Fig. 5. The theoretical capacity of NFM is estimated to be 240 $mAhg^{-1}$. As shown in Fig. 5, in the voltage window of 2.0–4.0 V, at C/10 rate, the reversible discharge capacity is measured to be 133 $mAhg^{-1}$ which corresponds to about 0.55 mol of Na^+ ion insertion. This is consistent of recent literature report. In this voltage window, the discharge capacity contributions are from Ni^{2+}/Ni^{4+} and Fe^{3+}/Fe^{4+} redox couples [30]. As shown in the inset, at 1C the discharge capacity drops down to 86 $mAhg^{-1}$, however, the capacity fades marginally till 50th charge – discharge galvanostatic cycling.

3.4. Electrochemical performance of 0.7 $Na_{0.44}MnO_2$ – 0.3 $Na(Ni_{1/3}Fe_{1/3}Mn_{1/3})O_2$ composite

The 1st and 10th cycle charge – discharge data of $0.7Na_{0.44}MnO_2$ – $0.3Na(Ni_{1/3}Fe_{1/3}Mn_{1/3})O_2$ (0.7NMO – 0.3NFM) is shown in Fig. 6(a). The 1st cycle charge capacity of the composite is measured to be 113 $mAhg^{-1}$. Considering the 1st cycle charge capacity of NMO and NFM are 96$mAhg^{-1}$ and 133 $mAhg^{-1}$, the 1st cycle charge capacity of the 0.7NMO–0.3NFM composite should be ~107 $mAhg^{-1}$ (=0.7×96+0.3×133 $mAhg^{-1}$). Thus, the measured capacity is marginally higher than the theoretical estimation for the composite cathode. The cycleability of the composite is shown in Fig. 6(b) measured at 1C rate. The capacity retention after 100 cycles is ~89.5 %. The charge–discharge profiles of the 10th, 50th and 100th cycles are shown in the inset of Fig. 6(b). Good reversibility is apparent in the shown figure. The rate performance of the composite in 3 C–15 C rate is shown in Fig. 6(c). The discharge capacity in 15C rate is reported to be ~66 $mAhg^{-1}$. A synergetic effect of NMO–NFM blended cathode materials on sodium ion transport for improved power performance is apparent. Thus, like that performed by Wu et al. [31], using Eqn. (1), we have calculated the capacity (Qc) and compared with the measured capacity (Q_m) of the blended cathode in half–cell configuration (see Table 2). Note that with the increase in rate (0.1C–1C), the difference of Q_m and Q_c is increased. This suggests a synergic effect in composite cathode.

$$Q_c = \frac{(m_{NMO}{}^*Q_{NMO} + m_{NFM}{}^*Q_{NFM})}{(m_{NMO} + m_{NFM})} = xQ_{NMO} + yQ_{NFM} \quad (1)$$

The synergetic effect becomes clearer in differential capacity plots. Thus, Fig. 7 compares the differential capacity plots of NMO and 0.7NMO – 0.3 NFM measured at (a) 0.1C and (b) 1C rate. For pure NFM the differential capacity plot is shown at the inset of Fig. 7(a). Comparing the differential capacity plots at 0.1C and 1C rates, we observe that all oxidations and reduction peaks are relatively broader and intense in the blended 0.7NMO-0.3NFM cathode. This effect is more prominent when the rate is increased (see Fig. 7(b)). Now consider the 5th differential capacity peaks from left (marked by small arrows). Comparing Fig. 7(a) and (b), with the increase in rate, the intensity of this differential capacity peak is significantly increased. Note that, as shown in the inset of Fig. 7(a), pure NFM does not exhibit any peak at this voltage (~3.25 V). Therefore, the increase in peak intensity of the composite, especially higher rate is indeed due to synergetic effect of the blended cathode. The surface morphology of the blended 0.7 NMO–0.3 NFM composite cathode is shown in Fig. 8. Since the morphology of NMO is distinctly different from NFM, by looking at the image, it is

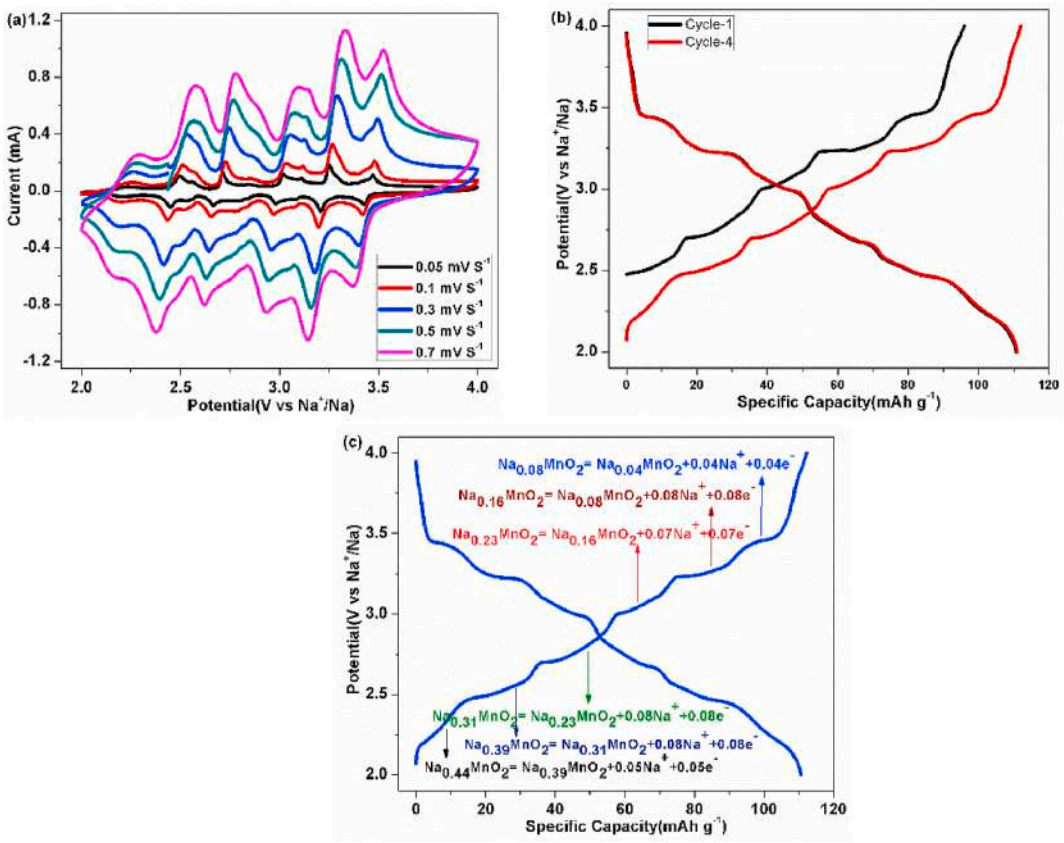

Fig. 4. (a) The cyclic voltammograms of $Na_{0.44}MnO_2$ measured in the voltage window of 2.0–4.0 V using voltage scan rates of 0.05–0.7 mVs^{-1}. (b) the charge discharge profiles of Na–$Na_{0.44}MnO_2$ half-cell at 1st and 4th charge – discharge cycles measured at C/10 rate. (c) The tentative electrochemical reactions corresponding to each plateau of the discharge profile.

Table-I
Electrochemical performance of different NMO cathodes for sodium ion battery.

Cathode materials	Synthesis technique	Initial charge capacity (mAh/g) At 0.1C	Reversible capacity with capacity retention	Reference
$Na_{0.44}MnO_2$	Solid state method with chemical pre-sodiation	115.7	110 mAh/g, 94.1 % over 200 cycle at 2C	[8]
$Na_{0.44}MnO_2$	Modified solid state method	110	115 mAh/g, 75 % over 400 cycles at 1C	[9]
$Na_{0.44}MnO_2$	Urea based auto combustion	62	111 mAh/g	[11]
$Na_{0.44}MnO_2$	Hydrothermal	60	110.7 mAh/g	[34]
Our Lab synthesized $Na_{0.44}MnO_2$	Modified auto combustion	96	110 mAh/g	

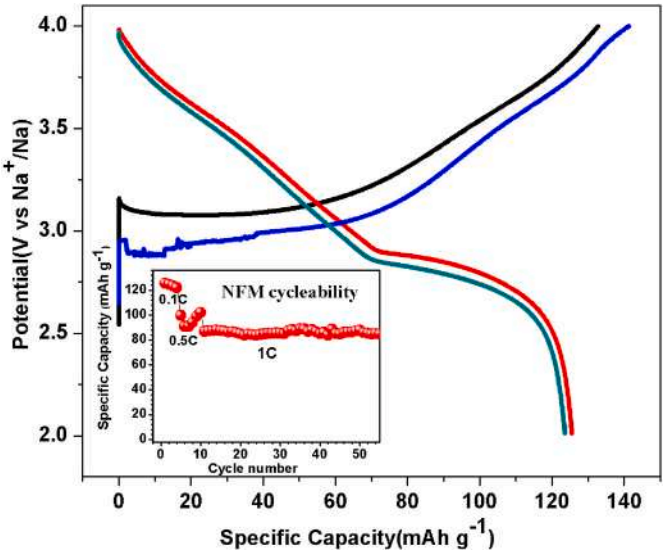

Fig. 5. The charge–discharge profile of TiO_2 coated Na $(Ni_{1/3}Fe_{1/3}Mn_{1/3})$ O_2 half cell in the voltage window of 2.0–4.0 V measured at C/10 rate. The inset shows the cycleability measured in 0.1 C to 1C rate.

apparent that these two components are mixed homogeneously with the binder in the composite cathode. Fig. 9 shows the Nyquist plots (symbols) of (a) pure NMO and (b) 0.7NMO–0.3NFM composite cathodes at fully discharged states. These Nyquist plots were fitted using equivalent circuits shown at the insets of Fig. 9. The high frequency semicircle is ascribed to the solid electrolyte interface layer (with resistance R2). The intermediate frequency semi-circle originates due to charge–transfer resistance in the cathode–electrolyte interface (R3). Constant phase elements (Q2 and Q3, connected parallel to R2 and R3) represent the depressed nature of these semicircles due to the roughness of the electrodes. The low frequency tail represents Na^+ ion diffusion (represented by Warbug impedance W4). The intercalation capacitance (C1) represents Na^+ ion occupation in the lattice sites [32,33]. For uniformly blended composite, as postulated by Wu et al. [31], the two components (NMO and NFM with resistances R_{NMO} and R_{NFM}) in the blend can be assumed to be connected in parallel to yield charge transfer resistance

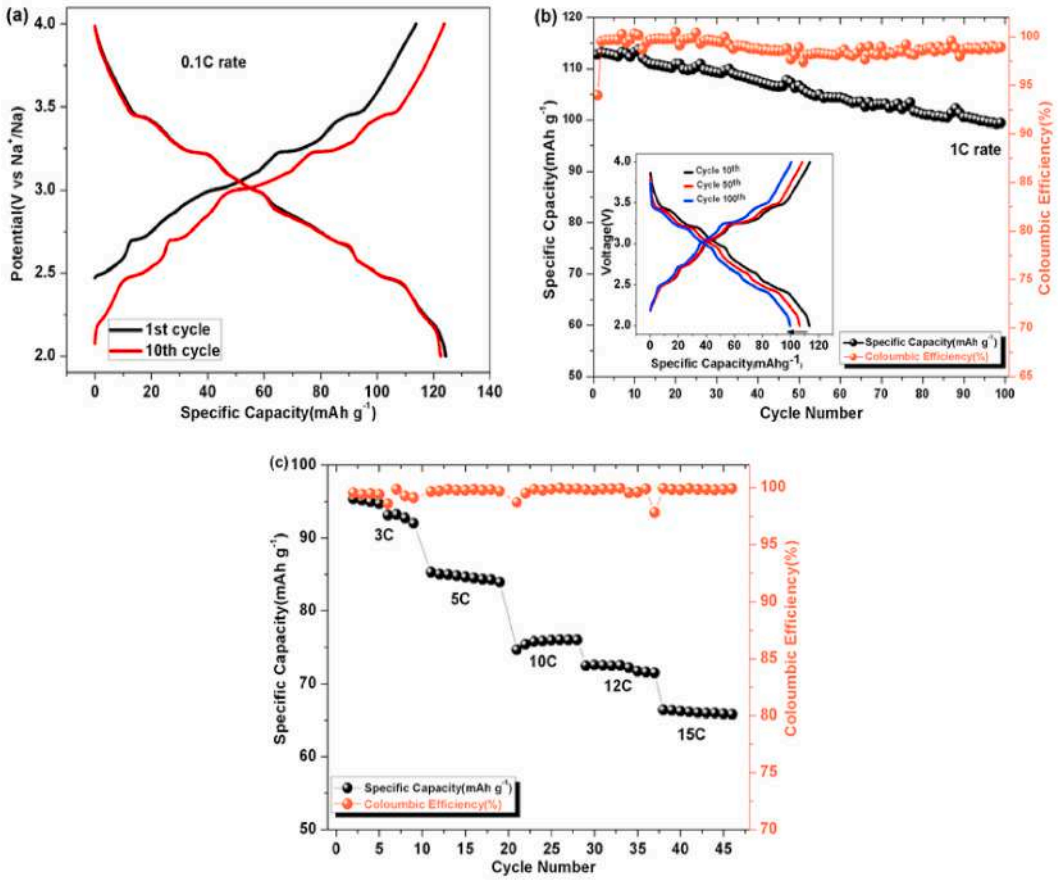

Fig. 6. (a) 1st and 10th charge–discharge profile of $0.7Na_{0.44}MnO_2 - 0.3Na\ (Ni_{1/3}Fe_{1/3}Mn_{1/3})\ O_2$ (0.7NMO – 0.3NFM) composite half– cell measured at 0.1 C rate. (b) the cycleability and Coulombic efficiency of the composite cathode measured at 1C rate. (c) the rate performance of the composite cathode measured in the range of 3C–15C rates.

Table 2
Comparison of measured and calculated capacity at 0.1C and 1C for composite and bare NMO cathode material.

Rate of discharge	Cathode	Q_m(mAh/g)	Q_c(mAh/g)	Q_m-Q_c(mAh/g)
0.1C	NMO	111	–	
0.1C	NFM	125	–	
0.1C	0.7NMO-0.3NFM	124	116	8
1C	NMO	98	–	
1C	NFM	82	–	
1C	0.7NMO-0.3NFM	110	93	17

(R_3) (=$R_{NMO}.R_{NFM}/(R_{NMO} + R_{NFM}$). As shown in Fig. 9, the simulated curve using the assumed equivalent circuit (solid line) fits quite well to the experimental data. The fitting parameters is tabulated in Table 3. Note that the R3 value (~9.42Ω) is significantly reduced in the composite as compared to its counterpart measured for pure NMO (~34.75Ω). This indicates superior Na^+ ion diffusion in NMO–NFM composite cathode as compared to bare NMO.

The diffusion coefficients are estimated from the relation

$$Z_{re} = R + \sigma\omega^{-1/2} \quad (2)$$

Where Z_{re} is the real impedance, ω is the frequency of the voltage applied in the EIS measurement, and R is the combination of all impedances in the system (~R_1+R_2+R_3). Fig. 10 shows the Z_{re} vs $\omega^{-1/2}$ plot for (a) NMO and (b) 0.7 NMO – 0.3 NFM composite cathodes (symbols). From the linear fit between Z_{re} vs $\omega^{-1/2}$ (solid line) we extracted the slope value σ. Subsequently from the estimated slope we calculated the diffusion coefficient (D^+_{Na}) using the following relation.

$$D^+_{Na} = \frac{0.5(RT)^2}{\left(An^2F^2c\sigma\right)^2} \quad (3)$$

Where R is the gas constant (8.314 J $K^{-1}mol^{-1}$), T is the absolute temperature (298.15 K), A is the working area of cathode (1.76 cm^2), n is the electronic transport ratio during redox process (n=1), F is the Faraday constant (96485.33 A s mol^{-1}), c is the concentration of sodium in $Na_{0.44}MnO_2$ cathode(1.87 × 10^{-3} mol/cm^3).

D^+_{Na} for bare NMO and 0.7NMO-0.3NFM is estimated to be 2.7 × 10^{-11} cm^2/s and 6.13 × 10^{-11} cm^2/s respectively. As expected the diffusion coefficient of Na^+ is indeed enhanced in the composite cathode.

Reviewing these results, we felt that the electrochemical performance of NMO–NFM composite needs to be investigated in full cell configuration using hard carbon and NMO/NFM composite as negative and positive electrode respectively. Table 4 compares the electrochemical performances of prepared $Na_{0.44}MnO_2$ with the ones reported in recent literatures. Facile synthesized $0.7Na_{0.44}MnO_2$– $0.3Na(Ni_{1/3}Fe_{1/3}Mn_{1/3})O_2$ (0.7NMO–0.3NFM) composite of the present work exhibits better electrochemical performances.

3.5. *Electrochemical performance of HC - 0.7 $Na_{0.44}MnO_2$ – 0.3 Na ($Ni_{1/3}Fe_{1/3}Mn_{1/3}$) O_2 (HC – NMO/NFM) full cell*

Limited attempts have so far been made to study the electrochemical

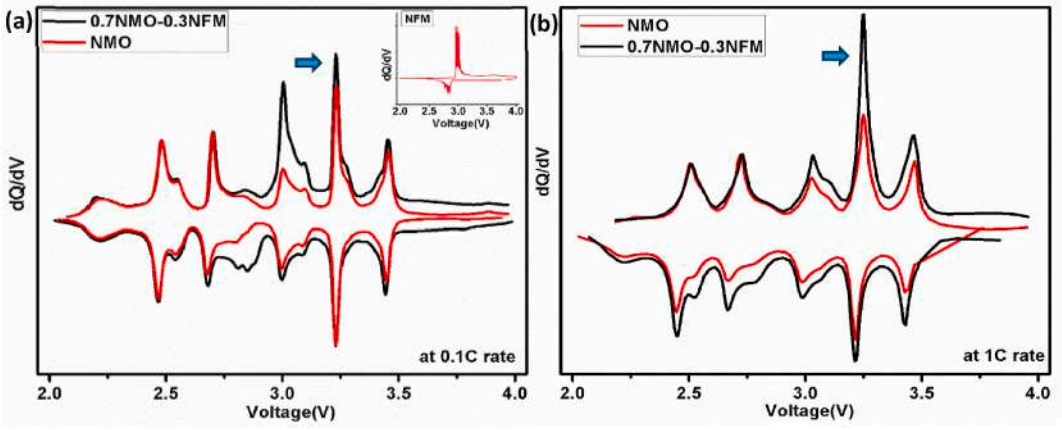

Fig. 7. (a) Differential capacity plot of 0.7 NMO-0.3NFM and NMO at 0.1C rate, and the inset shows about same for pure NFM at 0.1C rate. (b) Differential capacity plot of 0.7 NMO-0.3NFM and NMO at 1C rate.

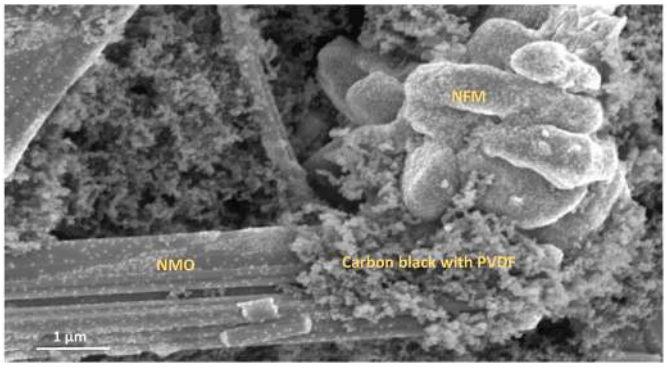

Fig. 8. Surface morphology of a composite electrode consisting of 0.7NMO and 0.3NFM, made with carbon black and PVDF in an 8:1:1 ratio.

performance of various composites made using tunnel type $Na_{0.44}MnO_2$ [33]. Zhang et al. [34] synthesized ball mill derived composite using hydrothermally synthesized $Na_{0.44}MnO_2$ and graphene. The initial discharge capacity was reported to be 106.9 $mAhg^{-1}$ at 50 mA/g rate. After 100 charge–discharge cycles a capacity retention ~85.9 % is reported. At 500 and 1000 mAg^{-1} the composite yields discharge capacities of 89 and 78 $mAhg^{-1}$. Thus, the composite is claimed to yield superior rate performance. No full cell characteristics have been reported for such composite. Zheng et al. [18] synthesized $Na_{0.44}MnO_2$. $Na_2Mn_3O_7$ heterojunction structure using sol–gel technique. It was claimed that such heterojunction structure was effective to improve the characteristics of $Na_2Mn_3O_7$. At 200 $mAhg^{-1}$ the initial discharge capacity of the heterojunction was reported to be 119 $mAhg^{-1}$ and after 100 cycles capacity retention of 88 % was reported. At 1000 mAg^{-1}, the discharge capacity ~72 $mAhg^{-1}$ was measured for these composites. The full cell characteristics of these composites were not reported. Oz et al. [6] adopted Co doping for Mn in $Na_{0.44}MnO_2$. Optimized Co doping yields co-existence of layered P2 phase along with tunnel type NMO. Co substitution was also instrumental to reduce the Jahn–Teller effect to suppress the structural degradation. The discharge capacity of such layered/tunnel composite was found to be 90 $mAhg^{-1}$. After 100 cycles at 0.3C rate a capacity retention 84 % is achieved in such composite. No full cell electrochemical characteristics have been reported

Table 3
The fitting parameters for the Nyquist plot depicted in Fig. 9. The electrical circuit is illustrated in the inset of Fig. 9.

Circuit element	For Bare NMO	For 0.7NMO-0.3NFM
R1	11.1Ω	8.302 Ω
Q2	8.729×10^{-6} F $s^{\alpha-1}$	12.91×10^{-6} F $s^{\alpha-1}$
R2	15.39Ω	23.13Ω
Q3	6.988×10^{-3} F $s^{\alpha-1}$	5.077×10^{-3} F $s^{\alpha-1}$
R3	34.75Ω	9.42Ω
W4	10.67 Ω $s^{-1/2}$	7.22 Ω $s^{-1/2}$
C1	1.38 F	2.53 F

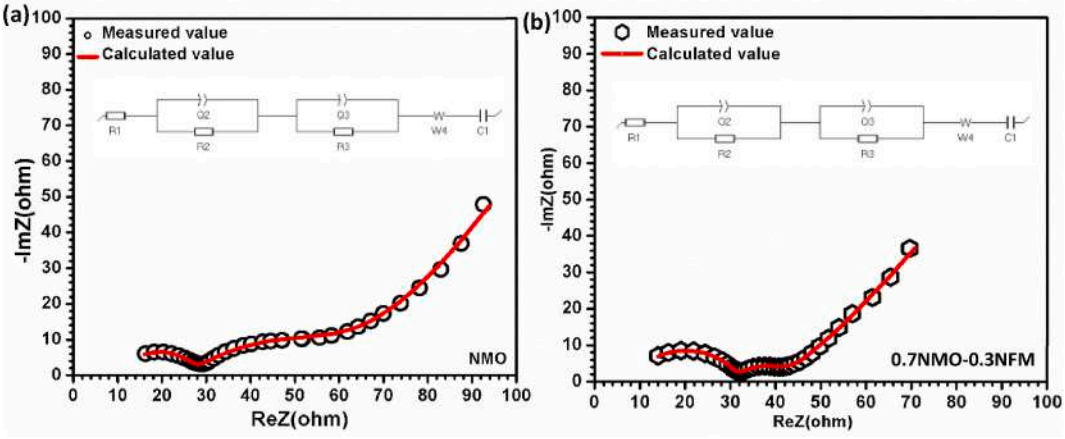

Fig. 9. Electrochemical impedance spectroscopy(Nyquist plot) of (a) NMO and (b) a 0.7NMO-0.3NFM blend electrode.Both the spectra was measured at a frequency range of 10 kHz to 10 mHz in coin cell format.

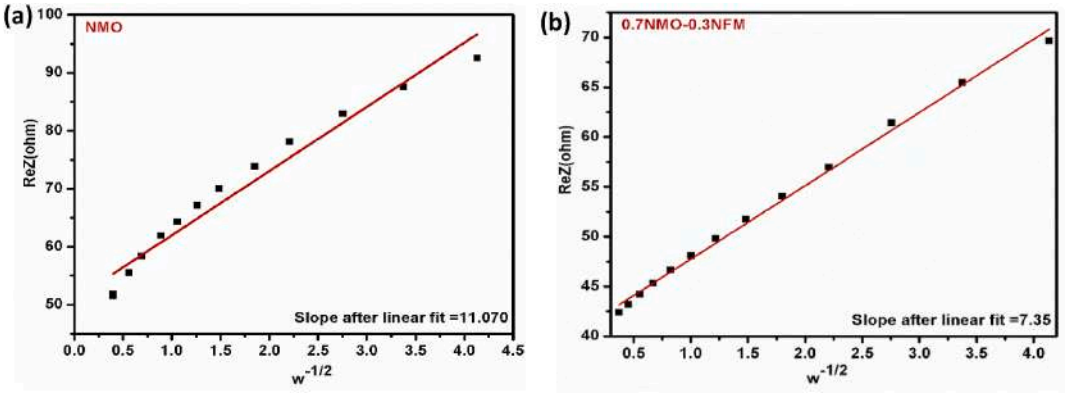

Fig. 10. Z_{re} vs. $\omega^{-1/2}$ plot at lower frequency region of Nyquist plot to determine the bulk diffusion coefficient (D^{+}_{Na}) within a material.

Table-IV
Electrochemical performance of different NMO Composite or sodium ion battery.

Cathode materials	Synthesis technique	Initial charge capacity (mAh/g) At 0.1C	Reversible capacity (mAh/g) with capacity retention	Rate performance	Reference
$Na_{0.44}MnO_2$-$Na_2Mn_3O_7$	Sol-gel assisted High temperature sintering	150 mAh/g (at 1.5–4.6 V Window)	278 mAh/g(at 1.5–4.6 V window)	72 mAh/g at 1000 mA/g	[18]
$Na_{0.44}Mn_{0.85}Ti_{0.15}O_2$-PBA	Modified solid state method and for PBA -Coprecipitation	110 mAh/g at 0.1C	115 75 % over 400 cycles at 1C	at 10C 60mAh/g	[17]
(Our lab synthesized) 0.7$Na_{0.44}MnO_2$-0.3NFM Composite	Modified Autocombustion followed by composite mixing	110 mAh/g at 0.1C	124 89.5 % after 100 cycle	at 15C 66 mAh/g	

for these composites. Liu et al. [17] made Prussian blue analogue (PBA)–$Na_{0.44}Mn_{1-x}Ti_xO_2$ composite for its commercial adaptation. PBA acted as complementary sodium source and offered Fe^{2+}/Fe^{3+} redox couples to contribute on capacity and cycling performance. In coin cell configuration full cell yields discharge capacity ~97.3mAhg^{-1} at 0.1C. Coulombic efficiency was reported to be 88.69 %. When cycled at 0.5C, capacity retention of 67.36 % was achieved after 300 cycles. These results can be compared to the electrochemical performance of the composite cathode based full cell investigated in the present work. The half–cell characteristics of HC is shown in conjunction with NMO–NFM composite (Fig. 11(a)) measured at C/10 rate. The mass balance of the respective electrodes was done (as far as practical) to construct the full cell. The N/P ratio, we have taken 0.9. In the voltage window between 1.0 and 4.0 V, Fig. 11(b) shows the charge discharge capacity of HC–NMO/NFM full cell measured at 1C. As shown in Fig. 11(b), 1st cycle charge capacity was ~112 mAhg^{-1} with corresponding discharge capacity ~ 109 mAhg^{-1}. Thus, increasing rate from 0.1C (133 mAhg^{-1}) to 1C (109mAhg^{-1}), the discharge capacity drops only ~ 18%. After 100 charge – discharge cycles at 1C the discharge capacity fades to 86 mAhg^{-1} (capacity retention ~80 %). Table 5 compares the electrochemical performances of prepared composite full cell with other composites reported in recent literatures. Facile synthesized hard carbon - 0.7$Na_{0.44}MnO_2$–0.3Na ($Ni_{1/3}Fe_{1/3}Mn_{1/3}$) O_2 (0.7NMO – 0.3NFM) full cell of the present work exhibits better electrochemical performances.

4. Summary and conclusions

By controlling the fuel: oxidizer ratio during auto–combustion synthesis we have been able to induce carbothermal reductive environment to preserve lamellar Birnessite type slab even after high temperature synthesis of tunnel structured $Na_{0.44}MnO_2$ powders. A stress induced mechanism was proposed to explain the splitting of the lamellar nanosheet to $Na_{0.44}MnO_2$ nanorods of various L/D ratios. Thus, during auto – combustion synthesis lamellar Birnessite formed as intermediate phase at temperature <400°C. Subsequently, during high temperature calcination, Mn^{3+} ions of Birnessite phase undergo a disproportionate

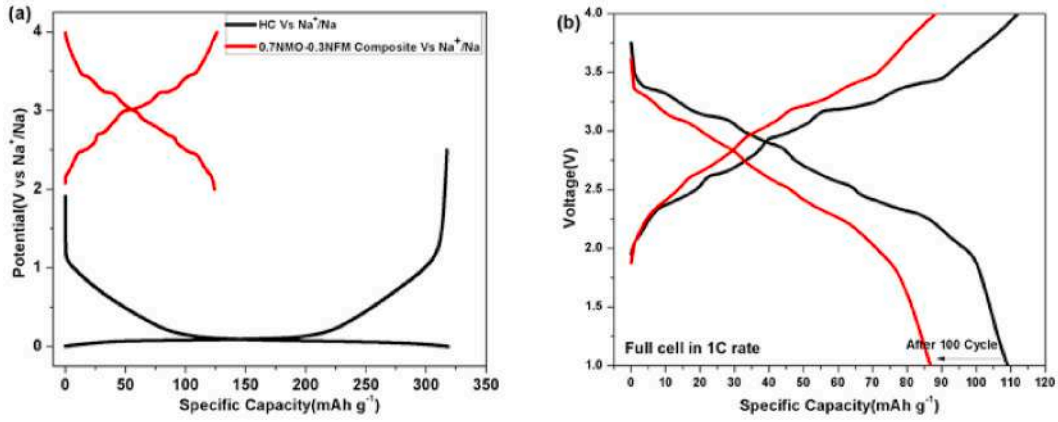

Fig. 11. (a) In the voltage window of 1.0–4.0 V, half – cell characteristics of hard carbon and 0.7NMO – 0.3 NFM measured at C/10 rate. (b) charge – discharge capacity of HC – 0.7NMO – 0.3NFM full cell measured after 1st and 100th cycles measured at 1C.

Table -V
Electrochemical performance of different $Na_{0.44}MnO_2$ Based full cell for sodium ion battery.

Cathode -Anode materials for full cell	Synthesis technique	Initial charge capacity (mAh/g)	Reversible capacity with capacity retention	C Rate	Reference
B doped $Na_{0.44}MnO_2$- HC	Oxalate mixture sintering	105	75	0.1C	[33]
[0.8$Na_{0.44}Mn_{0.85}Ti_{0.15}O_2$-0.2PBA] -HC Full cell	Modified solid state method and for PBA -Coprecipitation	110	97	0.1C	[17]
(Our lab synthesized) [0.7$Na_{0.44}MnO_2$-0.3NFM Composite]-HC full cell	Modified Autocombustion followed by composite mixing	112	109	1C	

reaction to form Mn^{4+} and Mn^{2+} ions. Mn^{2+} ions and oxidized during calcination in air ambient to form shared MnO_6 octahedra and the induced strain weakens the Birnessite layers. Eventually, due to the in-plane stress, high density of defects and stacking fault the nano sheet splits into nanorods. Transmission microscopy analyses confirm the growth direction of the sheet is different from the direction of Na^+ extraction/insertion. The diffusion distance for Na^+ ion extraction is much shorter than the growth direction to facilitate the extraction of beyond 0.22 Na^+ from the $Na_{0.44}MnO_2$ lattice. Due to facile extraction of Na^+ ions from Na2, Na3 as well as Na1 sites, a remarkable 1st charge capacity as high as 96 $mAhg^{-1}$ has been reported in a tunnel-type $Na_{0.44}MnO_2$ cathode. Composite of $Na_{0.44}MnO_2$ (NMO) and TiO_2 coated Na ($Ni_{1/3}Fe_{1/3}Mn_{1/3}O_2$)(NFM) was made as a novel cathode for Na ion rechargeable cells. As demonstrated, auto–combustion synthesized NMO favours facile Na^+ ion diffusion to improve rate performance and in conjunction it acts as a pillar to retard structural degradation of commercial TiO_2 coated NFM to improve the cycleability of the composite. At 1C rate the discharge capacity of 0.7 NMO–0.3 NFM composite is reported to be 113 $mAhg^{-1}$ with a capacity retention of ~80% after 100 charge–discharge cycles. The composite cathode also exhibits superior rate performance with a discharge capacity ~66 $mAhg^{-1}$ at 15C rate. Full cell was fabricated using hard carbon as negative and NMO–NFM composite as positive electrode. In a voltage window of 1.0–4.0 V, the discharge capacity of the full cell was measured to be 133 $mAhg^{-1}$ and 109 $mAhg^{-1}$ at 0.1 and 1C respectively. After 100 cycles, at 1C rate we have reported 80% capacity retention of the full cell.

CRediT authorship contribution statement

Soutan Adak: Writing – original draft, Data curation. **Ahin Roy:** Formal analysis. **Susanta Banerjee:** Formal analysis. **Jeng-Kuei Chang:** Investigation. **Subhasish Basu Majumder:** Writing – review & editing, Supervision, Project administration, Methodology, Funding acquisition, Formal analysis, Conceptualization.

Declaration of competing interest

The authors declare the following financial interests/personal relationships which may be considered as potential competing interests: Subhasish Basu Majumder reports financial support was provided by Tata Chemical Society for Rural Development, near town office, Mitahpur - 361345, Taluka, Okhamandal, Dist Devbhoomi Dwaraka, Gujrat. Subhasish Basu Majumder reports a relationship with Indian Institute of Technology Kharagpur that includes: employment. If there are other authors, they declare that they have no known competing financial interests or personal relationships that could have appeared to influence the work reported in this paper.

Acknowledgement

SBM gratefully acknowledges partial funding received from Tata Chemicals Society for Rural Development (TCSRD) vide grant no: PONIB001. SA and SBM acknowledge the DST-funded FIST facility for FESEM. AR acknowledges the DST-funded SATHI facility, established and maintained by SATHI Foundation at IIT Kharagpur for HRTEM imaging. AR also acknowledges the funding under DAE-BRNS, Government of India, for the beamtime to carry out the imaging.

Appendix A. Supplementary data

Supplementary data to this article can be found online at https://doi.org/10.1016/j.jpowsour.2025.238413.

Data availability

Data will be made available on request.

References

[1] P. Phogat, S. Dey, M. Wan, Comprehensive review of sodium-ion batteries: principles, materials, performance, challenges, and future perspectives, Mater. Sci. Eng., B 312 (2025) 117870.
[2] H. Kim, D.J. Kim, D.H. Seo, M.S. Yeom, K. Kang, D.K. Kim, Y. Jung, Ab initio study of the sodium intercalation and intermediate phases in $Na_{0.44}MnO_2$ for sodium-ion battery, Chem. Mater. 24 (2012) 1205.
[3] W. Xu, L. Jiang, Y. Li, J. Zhang, Q. Huang, J. Yao, S. Xiao, C. Lei, Sodium storage performance and mechanism of MnO_2 with different phase structures (α, β, γ, δ) as anode materials for sodium-ion batteries, ACS Appl. Mater. Interfaces 16 (2024) 61877.
[4] X. Zhou, A. Zhao, Z. Chen, Y. Cao, Research progress of tunnel-structural $Na_{0.44}MnO_2$ cathode for sodium-ion batteries: a mini review, Electrochem. Commun. 122 (2021) 106897.
[5] F. Sauvage, L. Laffont, J.M. Tarascon, E. Baudrin, Study of the insertion/deinsertion mechanism of sodium into $Na_{0.44}MnO_2$, Inorg. Chem. 46 (2007) 3289.
[6] E. Oz, S. Altin, S. Avci, Tunnel/layer composite $Na_{0.44}MnO_2$ cathode material with enhanced structural stability via cobalt doping for sodium-ion batteries, ACS Omega 8 (2023) 27170.
[7] R.R. Kapaev, S. Chakrabarty, A. Mukherjee, M. Sonoo, M. Noked, Mild and fast chemical presodiation of $Na_{0.44}MnO_2$, J. Electrochem. Soc. 171 (2024) 070541.
[8] X. Zhou, Y. Lai, X. Wu, Z. Chen, Z. Faping, A.I. Xinping, Y. Hanxi, C.A.O. Yuliang, Improved initial charging capacity of Na-poor $Na_{0.44}MnO_2$ via chemical presodiation strategy for low-cost sodium-ion batteries, Chem. Res. Chin. Univ. 37 (2021) 274.
[9] S. Chakrabarty, J.A. Dar, A. Joshi, A. Paperni, S. Taragin, A. Maddegalla, G. Sai Gautam, A. Mukherjee, M. Noked, Unveiling the structural integrity of tunnel-type $Na_{0.44}MnO_2$ cathode for sodium ion battery, J. Mater. Chem. A Mater. 12 (2024) 25109.
[10] D. Wang, L. Teng, W. Liu, Mn-based tunnel-structured $Na_{0.44}MnO_2$ cathode materials for high-performance sodium-ion batteries: electrochemical mechanism, synthesis and modifications, Chem. Commun. 1 (2024) 803.
[11] N. Sheng, C. gong Han, Y. Lei, C. Zhu, Controlled synthesis of $Na_{0.44}MnO_2$ cathode material for sodium ion batteries with superior performance through urea-based solution combustion synthesis, Electrochim. Acta 283 (2018) 1560.
[12] W. Ni, Q. Ding, W. Zheng, G. Peng, H. Wang, Z. Xie, Y. Cao, A W/Al Co-doped $Na_{0.44}MnO_2$ cathode material for enhanced sodium-ion storage, ACS Appl. Mater. Interfaces 16 (2024) 64725.
[13] T. Liebmann, C. Heubner, M. Schneider, A. Michaelis, Understanding kinetic and thermodynamic properties of blended cathode materials for lithium-ion batteries, Mater. Today Energy 22 (2021) 100845.
[14] D. Chatzogiannakis, M. Fehse, M.A. Cabañero, N. Romano, A. Black, D. Saurel, M. R. Palacin, M. Casas-Cabanas, Towards understanding the functional mechanism and synergistic effects of $LiMn_2O_4$ - $LiNi_{0.5}Mn_{0.3}Co_{0.2}O_2$ blended positive electrodes for lithium-ion batteries, J. Power Sources 591 (2023) 233804.
[15] J. Yao, M. Xu, Y. Li, B. Huang, J. Yang, Facile preparation of $Fe_3O_4/ZnFe_2O_4/ZnS$/C composite from the leaching liquor of jarosite residue as a high-performance anode material for Li-ion batteries, J. Alloys Compd. 952 (2023) 169993.
[16] J. Yao, T. Yu, Q. Huang, Y. Li, B. Huang, J. Yang, Preparation of Mn_2O_3/Fe_2O_3 composite cathode material for zinc ion batteries from the reduction leaching solution of manganese ore tailing, J. Ind. Eng. Chem. 136 (2024) 524.
[17] H. Liu, L. Kong, H. Wang, J. Li, J. Wang, Y. Zhu, H. Li, Z. Jian, X. Jia, Y. Su, S. Zhang, J. Mao, S. Chen, Y. Liu, S. Chou, Y. Xiao, Reviving sodium tunnel oxide cathodes based on structural modulation and sodium compensation strategy toward practical sodium-ion cylindrical battery, Adv. Mater. 36 (2024) 2407994.

[18] P. Zheng, J. Su, Y. Wang, W. Zhou, J. Song, Q. Su, N. Reeves- McLaren, S. Guo, A high-performance primary nanosheet heterojunction cathode composed of $Na_{0.44}MnO_2$ tunnels and layered $Na_2Mn_3O_7$ for Na-Ion batteries, ChemSusChem 13 (2020) 1793.
[19] J. Wang, Q. Sun, J. Yu, J. Guo, N. Mo, H. Li, Y. Su, S. Zhao, Y. Zhu, H. Chu, S. Dou, Y. Xiao, Constructing layered/tunnel interlocking oxide cathodes for sodium-ion batteries based on breaking Mn^{3+}/Mn^{4+} equilibrium in $Na_{0.44}MnO_2$ via trace Mo doping, Compos. B Eng. 284 (2024) 111664.
[20] J. Cai, Y. Zhu, Z. Zhang, J. Zhang, L. Tian, P. Gao, Y. Zhang, M. Wang, Y. Shen, Electronic modification of $NaCrO_2$ via Ni^{2+} substitution as efficient cathode for sodium-ion batteries, Energy Mater. 4 (2024) 400073.
[21] D. Kim, E. Lee, M. Slater, W. Lu, S. Rood, C.S. Johnson, Layered $Na[Ni_{1/3}Fe_{1/3}Mn_{1/3}]O_2$ cathodes for Na-ion battery application, Electrochem. Commun. 18 (2012) 66.
[22] X. He, J. Wang, B. Qiu, E. Paillard, C. Ma, X. Cao, H. Liu, M.C. Stan, H. Liu, T. Gallash, Y.S. Meng, J. Li, Durable high-rate capability $Na_{0.44}MnO_2$ cathode material for sodium-ion batteries, Nano Energy 27 (2016) 602.
[23] Y. Li, Y. Wu, Formation of $Na_{0.44}MnO_2$ nanowires via stress-induced splitting of birnessite nanosheets, Nano Res. 2 (2009) 54.
[24] P. Le Goff, N. Baffier, S. Bach, J.P. Pereira-Ramos, R. Messina, Structural and electrochemical characteristics of a lamellar sodium manganese oxide synthesized via a sol-gel process, Solid State Ionics 61 (1993) 309.
[25] M. Xu, Y. Niu, C. Chen, Ji Song, S. Bao, C.M. Li, Synthesis and application of ultra-long $Na_{0.44}MnO_2$ submicron slabs as a cathode material for Na-ion batteries, RSC Adv. 4 (2014) 38140.
[26] C. Liu, J. Li, P. Zhao, W. Guo, X. Yang, Fast preparation of $Na_{0.44}MnO_2$ nanorods via a high NaOH concentration hydrothermal soft chemical reaction and their lithium storage properties, J. Nanoparticle Res. 17 (2015) 142.
[27] P. Zhan, S. Wang, Y. Yuan, K. Jiao, S. Jiao, Facile synthesis of nanorod-like single crystalline $Na_{0.44}MnO_2$ for high performance sodium-ion batteries, J. Electrochem. Soc. 162 (2015) A1028.
[28] M.S. Chae, H.J. Kim, H. Bu, J. Lyoo, R. Attias, B. Dlugatch, M. Oliel, Y. Gofer, H. T. Hong, D. Aurbach, The sodium storage mechanism in tunnel-type $Na_{0.44}MnO_2$ cathodes and the way to ensure their durable operation, Adv. Energy Mater. 10 (2020) 2000564.
[29] C. Delmas, J.-J. Braconnier, C. Fouassier, P. Hagenmuller, Electrochemical intercalation of sodium in Na_xCoO_2 bronzes, Solid State Ionics 3 (1981) 165.
[30] M. Jeong, H. Lee, J. Yoon, W.S. Yoon, O3-type $NaNi_{1/3}Fe_{1/3}Mn_{1/3}O_2$ layered cathode for Na-ion batteries: structural evolution and redox mechanism upon Na (de) intercalation, J. Power Sources 439 (2019) 227064.
[31] D. Wu, H. Ren, Y. Guo, X. Zhang, Z. Zhang, J. Li, Synergetic effects of $LiNi_{1/3}Co_{1/3}Mn_{1/3}O_2 - LiMn_2O_4$ blended materials on lithium ionic transport for power performance, Ionics 25 (2018) 1595.
[32] M.D. Levi, G. Salitra, B. Markovsky, H. Teller, D. Aurbach, U. Heider, L. Heider, Solid-state electrochemical kinetics of Li-ion intercalation into $Li_{1-x}CoO_2$: simultaneous application of electroanalytical techniques SSCV, PITT, and EIS, J. Electrochem. Soc. 146 (1999) 1279.
[33] Z.M. Liu, X.T. Feng, H.J. Zhao, X.Q. Han, Z.X. Ye, Z. Ca Yao, D. Zhang, High-performance B-Doped $Na_{0.44}MnO_2$ cathode materials for sodium-ion batteries, ACS Omega 10 (2025) 10023.
[34] Y. Zhang, Y. Ouyang, L. Liu, J. Xia, S. Nie, W. Liu, X.Y. Wang, Synthesis and characterization of $Na_{0.44}MnO_2$ nanorods/graphene composite as cathode materials for sodium-ion batteries, J. Cent. South Univ. 26 (2019) 1510.